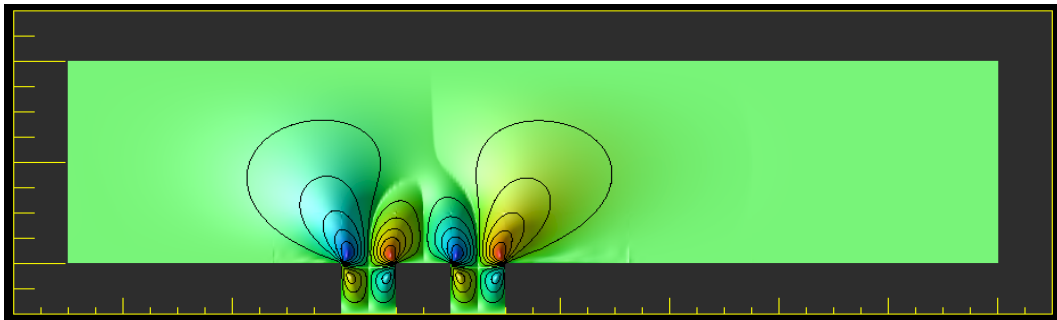


# NUMERICAL PREDICTION OF THE HYPERSONIC BOUNDARY-LAYER OVER A ROW OF MICROCAVITIES



VASSILIOS THEOFILIS  
F61775-01-WE049 FINAL REPORT  
SEPTEMBER 2002

<b>REPORT DOCUMENTATION PAGE</b>				Form Approved OMB No. 0704-0188	
<p>Public reporting burden for this collection of information is estimated to average 1 hour per response, including the time for reviewing instructions, searching existing data sources, gathering and maintaining the data needed, and completing and reviewing the collection of information. Send comments regarding this burden estimate or any other aspect of this collection of information, including suggestions for reducing the burden, to Department of Defense, Washington Headquarters Services, Directorate for Information Operations and Reports (0704-0188), 1215 Jefferson Davis Highway, Suite 1204, Arlington, VA 22202-4302. Respondents should be aware that notwithstanding any other provision of law, no person shall be subject to any penalty for failing to comply with a collection of information if it does not display a currently valid OMB control number.</p> <p><b>PLEASE DO NOT RETURN YOUR FORM TO THE ABOVE ADDRESS.</b></p>					
<b>1. REPORT DATE (DD-MM-YYYY)</b> 02-12-2002		<b>2. REPORT TYPE</b> Final Report		<b>3. DATES COVERED (From – To)</b> 12 June 2001 - 12-Jun-02	
<b>4. TITLE AND SUBTITLE</b>  Numerical Prediction Of The Hypersonic Boundary-Layer Over A Row Of Microcavities			<b>5a. CONTRACT NUMBER</b> F61775-01-WE049		
			<b>5b. GRANT NUMBER</b>		
			<b>5c. PROGRAM ELEMENT NUMBER</b>		
<b>6. AUTHOR(S)</b>  Dr. Vassilios Theofilis			<b>5d. PROJECT NUMBER</b>		
			<b>5d. TASK NUMBER</b>		
			<b>5e. WORK UNIT NUMBER</b>		
<b>7. PERFORMING ORGANIZATION NAME(S) AND ADDRESS(ES)</b> Nu-modeling, Inc. Rohnsterrassen 14 Gottingen D-37085 Germany				<b>8. PERFORMING ORGANIZATION REPORT NUMBER</b>  N/A	
<b>9. SPONSORING/MONITORING AGENCY NAME(S) AND ADDRESS(ES)</b>  EOARD PSC 802 BOX 14 FPO 09499-0014				<b>10. SPONSOR/MONITOR'S ACRONYM(S)</b>	
				<b>11. SPONSOR/MONITOR'S REPORT NUMBER(S)</b> SPC 01-4049	
<b>12. DISTRIBUTION/AVAILABILITY STATEMENT</b>  Approved for public release; distribution is unlimited.					
<b>13. SUPPLEMENTARY NOTES</b>					
<b>14. ABSTRACT</b>  This report results from a contract tasking Nu-modeling, Inc. as follows: The contractor will perform detailed numerical predictions of the flowfield in the neighborhood of the microcavities that are embedded in wall-coatings. The key deliverable of the proposed work will be the ability to put forward an improved integral condition to replace what is used in the current theoretical approach. This will be determined numerically at each of the parameters of the problem. The numerical effort required for the solution of the problem at a single value of each of the parameters involved limits to subset of the (M, Re, m, d, d/D, d/s) parameter space that can be investigated within the available year. It is intended to approximate existing analytic results of Fedorov first, at a single set of parameters, by imposing his pressure boundary condition at the lips of the microcavities (i.e. taking D=0). The effect of nonzero values of this parameter will then be examined, keeping all other parameters in the problem constant. Subsequently, the effect of d, and s will be investigated, at constant D and 2(d+s). In all D <sup>1</sup> 0 cases to be studied, integral boundary conditions will be provided to the parties involved in the project. Progress of the proposed research will be monitored by means of one intermediate and one final report.					
<b>15. SUBJECT TERMS</b> EOARD, Boundary Layer, Hypersonic Flow, CFD, Computational Aerodynamics, Cavity Acoustics, Transition					
<b>16. SECURITY CLASSIFICATION OF:</b>			<b>17. LIMITATION OF ABSTRACT</b> UL	<b>18. NUMBER OF PAGES</b>  33	<b>19a. NAME OF RESPONSIBLE PERSON</b> Wayne Donaldson
<b>a. REPORT UNCLAS</b>	<b>b. ABSTRACT UNCLAS</b>	<b>c. THIS PAGE UNCLAS</b>			<b>19b. TELEPHONE NUMBER</b> (Include area code) +44 (0)20 7514 4299

# Numerical prediction of the hypersonic boundary-layer over a row of microcavities

BY VASSILIOS THEOFILIS †

*Rohnsterrassen 14, D-37085 Göttingen, GERMANY*

tel./fax: +49 551 48 76 25 vassilios.theofilis@nu-modelling.com <http://www.nu-modelling.com>

The present effort has addressed the issue of stabilization of hypersonic boundary layer flow on account of porous coating of the wall, a phenomenon discovered by Fedorov & Malmuth (2001) and demonstrated experimentally by Rasheed *et al.* (2001). Two aspects of the problem have been considered numerically, recovery of two-dimensional, essentially nonparallel basic states and three-dimensional BiGlobal instability analysis of such basic states. A set of two-dimensional direct numerical simulations have addressed slow flow inside a single or a pair of microcavities embedded in the wall. An efficient algorithm has been presented for the recovery of basic states in isolated cavities, driven by constant shear, with or without superimposed small-amplitude perturbations originating in the boundary layer. Further, the essential modification of the boundary layer flow in the presence of a row of microcavities has been documented using spectral-element DNS. Parameter ranges have been identified within which it is permissible to employ simplified models to describe flow in a single microcavity and calculate the effect on the boundary layer flow in an analytic, integral manner. Finally, BiGlobal instability analysis has revealed analogies in the most unstable eigenmodes of the shear-driven and the lid-driven cavity flow (Theofilis, 2000*a*). Research directions in the continuing quest to guide associated experimental efforts to control hypersonic boundary layer flow have been proposed.

† This material is based upon work supported by the European Office of Aerospace Research and Development, Air Force Office of Scientific Research, Air Force Research Laboratory, under Contract No. F61775-01-WE049 monitored by Dr. John D. Schmisser.

## **Contents**

1. Introduction/Theoretical aspects	4
2. Numerical methods	6
(a) Single cavity, steady runs	7
(b) Single cavity, unsteady runs	9
(c) Row of microcavities, unsteady runs	9
3. Results	11
(a) Basic flow	11
(b) Global linear instability	14
4. Conclusions	16

## 1. Introduction/Theoretical aspects

The motivation for the present study is in the development of a better understanding of the flow inside porous coatings which have recently been shown to have very beneficial effects in controlling hypersonic boundary-layer instabilities (Fedorov & Malmuth, 2001; Rasheed *et al.*, 2001). In the present model, two-dimensional cavities are considered and a non-parallel (global) linear instability analysis of unsteady three-dimensional disturbances developing upon the laminar steady flow inside an isolated cavity is performed. The analysis is distinct from the plethora of approaches which monitor the instability of the shear-layer formed at the forward lip of the cavity, and is akin to spatial direct numerical simulation in that two spatial directions, those which define a two-dimensional cavity, are resolved while the third is taken as homogeneous and resolved by a Fourier expansion. The ability to resolve two spatial dimensions in the global eigenproblem permits a proper and rational treatment of factors affecting flow instability, such as variable aspect ratio, different heights of forward/rearward wall of the cavity and spacing between cavities. This approach is parallel to the effort of Duck (2002) who monitors the external flowfield inside the boundary layer; the link between the two approaches is provided by the boundary conditions at the open end of the cavities. The objective of the analyses is to determine global three-dimensional linear perturbations and the frequencies of such disturbances in a quest to guide associated experimental efforts to control the entire flowfield.

Interest in BiGlobal instability of this boundary layer has been raised by the discovery of Fedorov & Malmuth (2001) and Rasheed *et al.* (2001), who have recently demonstrated theoretically and experimentally, respectively, that mode II instability, which prevails in hypersonic boundary-layer flow under a variety of environmental conditions, can be effectively controlled passively by coating the surface on which the instability develops by a porous material. The objective of the present effort is to provide detailed numerical predictions of the flowfield in the neighbourhood of this porous material. The key feature of this technology is the large disparity of scales between a typical mode II wavelength and the diameter of each of the microscopic cavities on the coating, schematically depicted in Figure 1. The porous material can thus be modelled by a row of cavities which are embedded in the wall-coating; the cavities are of small size compared with the thickness of the boundary layer and are referred to as *microcavities*. The optimal distribution of the microcavities on the coating surface is currently limited by the unknown nature of the interaction between the flowfields in the immediate vicinity of neighbouring microcavities. The present effort addresses this issue by monitoring separately the flow regimes firstly in the boundary layer over the porous wall and secondly inside the microcavity with the aim to arrive at theoretically founded predictions on control of mode-II-driven laminar-turbulent transition in this configuration. The boundary condition at the wall of the boundary layer is used to provide the link between the two flow regimes. The flow inside the boundary layer and its instability characteristics are discussed in the related effort of Duck (2002); he argues firstly that, the flow inside the microcavity is expected to be of a viscous nature, driven by a constant shear at the open end of the microcavity and, secondly, that an incompressible model may be used for the description of the basic state inside the microcavities. The focus of the present numerical effort is on the description of the flowfield inside a single microcavity in isolation as well as in the basic flow in the near-wall region of a boundary layer in which the minimum nontrivial number of two microcavities is embedded into the wall.

Specifically, a number of simplifications can be employed in order to gain first insights into the configuration at hand. Those pertaining to the external boundary layer flow are discussed by Duck (2002); here we concentrate on the simplifications of the flowfield inside the microcavities. These amount to neglecting the three-dimensionality of the geometry for the purposes of the present effort as far as the basic state is concerned. Regarding global instabilities, a Fourier decomposition of the spanwise spatial direction is considered. As has been mentioned, the flow inside the microcavity is essentially incompressible driven by constant shear, which leaves two parameters to be considered besides Reynolds number, namely the length over the depth of each microcavity and the spacing between two neighbouring microcavities. In the absence of prior information on the flow at hand, here we focus on the basic state inside a single microcavity and its global instability. The latter is contrasted with that in the classic lid-driven cavity (Theofilis, 2000a).

The basic flow is calculated by numerical solution of the vorticity transport equation alongside the

relation between streamfunction and vorticity,

$$\frac{\partial \zeta}{\partial t} + \left\{ \frac{\partial \psi}{\partial y} \frac{\partial \zeta}{\partial x} - \frac{\partial \psi}{\partial x} \frac{\partial \zeta}{\partial y} \right\} - \mathcal{K} \zeta = 0, \quad (1.1)$$

$$\mathcal{K} \psi + \frac{1}{Re} \zeta = 0, \quad (1.2)$$

where  $\mathcal{K} = (1/Re) (\mathcal{D}_x^2 + \mathcal{D}_y^2)$ , while  $\zeta = -\partial \bar{u}/\partial y + \partial \bar{v}/\partial x$  is the vorticity of the basic flow and  $\psi$  is its streamfunction, for which  $\bar{u} = \partial \psi / \partial y$  and  $\bar{v} = -\partial \psi / \partial x$  holds. An efficient direct numerical simulation algorithm for the solution of (1.1-1.2) is presented in the next chapter.

A constant shear is imposed at the open lip of a single microcavity and two distinct situations are considered, one in which the equations of motion (1.1-1.2) are integrated in time until convergence to a steady state, and one in which such a state is perturbed harmonically on account of linear instability originating in the boundary layer. However, both basic flows obtained in this manner suffer from the restrictive assumption of prescribed (and limited) communication between flow in the boundary layer and the microcavity. Furthermore, interaction between the microcavities, which represents one of the main interests of the present research, cannot be addressed by monitoring microcavities in isolation. The influence of variation of geometric parameters of individual microcavities on the induced flowfield inside the boundary layer (and, consequently, on the stability characteristics of the flow) is a further issue worthy of investigation. Finally, despite the low Reynolds numbers encountered, it is by no means clear that the flow in the neighbourhood of the microcavities remains steady in the parameter range of interest. In order to address all these issues, basic states have also been obtained, considering the entire domain encompassing the near-wall portion of the boundary layer and a nontrivial minimum of two microcavities embedded in the wall.

BiGlobal instability analysis of the flow is addressed by numerical solution of the linear eigenvalue problem (Theofilis, 2002) in which the linear disturbance equations can be recast after substitution of a decomposition into the two-dimensional  $O(1)$  basic quantities  $\bar{\mathbf{q}} = (\bar{u}, \bar{v}, 0, \bar{p})^T$  and three-dimensional  $O(\varepsilon)$  disturbance quantities  $\tilde{\mathbf{q}} = \hat{\mathbf{q}}(x, y) e^{i\{\beta z - \Omega t\}}$ , with  $\hat{\mathbf{q}} = (\hat{u}, \hat{v}, \hat{w}, \hat{p})^T$  into the equations of motion, subtraction of the basic flow terms and neglecting terms at  $O(\varepsilon^2)$ . In the present temporal framework  $\beta$  is taken to be a real wavenumber parameter describing an eigenmode in the  $z$ -direction and solve for the complex eigenvalue  $\Omega$ .  $\Omega_r \equiv \Re\{\Omega\}$ , the real part of the eigenvalue is related with the frequency of the global eigenmode while the imaginary part is its growth/damping rate; a positive value of  $\Omega_i \equiv \Im\{\Omega\}$  indicates exponential growth of the instability mode  $\tilde{\mathbf{q}}$  in time  $t$  while  $\Omega_i < 0$  denotes decay of  $\tilde{\mathbf{q}}$  in time. When the wavenumber vector  $\beta \mathbf{e}_z$  is perpendicular to the plane on which the basic flow  $(\bar{u}, \bar{v}, 0, \bar{p})$  develops, as the case is in the present basic flow, it is possible to simplify the two-dimensional eigenvalue problem by rewriting it as one with real coefficients, which requires half the amount of storage compared with the standard form (Theofilis *et al.*, 2001). The absence of a basic flow  $z$ -velocity component in the linear operator in conjunction of the redefinitions

$$\tilde{\Omega} = i \Omega, \quad (1.3)$$

$$\tilde{w} = i \hat{w} \quad (1.4)$$

result in the following generalised real nonsymmetric partial derivative EVP after linearisation and subtraction of the basic-flow related terms.

$$[\mathcal{M} - (\mathcal{D}_x \bar{u})] \hat{u} - (\mathcal{D}_y \bar{u}) \hat{v} - \mathcal{D}_x \hat{p} = \tilde{\Omega} \hat{u}, \quad (1.5)$$

$$-(\mathcal{D}_x \bar{v}) \hat{u} + [\mathcal{M} - (\mathcal{D}_y \bar{v})] \hat{v} - \mathcal{D}_y \hat{p} = \tilde{\Omega} \hat{v}, \quad (1.6)$$

$$+\mathcal{M} \tilde{w} - \beta \hat{p} = \tilde{\Omega} \tilde{w}, \quad (1.7)$$

$$\mathcal{D}_x \hat{u} + \mathcal{D}_y \hat{v} - \beta \tilde{w} = 0, \quad (1.8)$$

where

$$\mathcal{M} = (1/Re) (\mathcal{D}_x^2 + \mathcal{D}_y^2 + \beta^2) - \bar{u} \mathcal{D}_x - \bar{v} \mathcal{D}_y. \quad (1.9)$$

The ability to solve a real eigenvalue problem is essential in the case of the present high Reynolds numbers flow. This point has been clearly manifested in the literature in the difficulties encountered by the investigators who tackled the problem of linear instability in the classic lid-driven cavity to produce consistent results.

## 2. Numerical methods

In a manner analogous to classic linear theory, in which one spatial direction is resolved and two are considered homogeneous and represented by Fourier expansions, the details of the basic state of a global linear instability analysis crucially condition the quality of the stability analysis results. For this reason effort has been paid to develop a novel *accurate* and *efficient* numerical approach for the calculation of the basic state, details of which are presented here.

The principles of the algorithm can be applied to recover three two-dimensional velocity components or indeed a three-dimensional flowfield (Ku *et al.*, 1987); however, for simplicity we confine the present discussion to solutions of the system (1.1-1.2) which deliver the basic flowfield,  $\bar{\mathbf{q}}$ , inside a two-dimensional rectangular microcavity. The main advantage of the velocity-vorticity formulation is that the continuity equation is exactly satisfied. However, the problem of imposition of boundary conditions within the framework of an overall efficient numerical solution algorithm remains. This is compounded by the fact that the number of points discretising the two spatial directions in the subsequent analysis cannot be increased at will; while interpolation of a basic flow solution obtained on a very large number of points onto a modest EVP grid is one possible option, it is more elegant to avoid the interpolation procedure altogether and seek an accurate basic flow solution on *the same* small number of discretisation points on which the subsequent global instability analysis is to be performed. This appears tailor-made for a spectral numerical solution approach (Canuto *et al.*, 1987); in what follows we discuss a different solution based on an efficient real-space eigenvalue decomposition (EVD) algorithm.

Chebyshev polynomials have almost exclusively been used in the past in the context of spectral simulations of the time-accurate Navier-Stokes and continuity equations, mainly due to the availability of fast transform algorithms necessary for efficient time-integration. However, for the present problems we have not restricted ourselves to this class of orthogonal polynomials. Considerable freedom exists in the choice of the expansion functions and the associated collocation grids by using Jacobi polynomials  $P^{(q,r)}$  for the discretization of both spatial directions; of course,  $q = r = -0.5$  may be related to the Chebyshev- while  $q = r = 0$  are the Legendre polynomials. Collocation derivative matrices for both Jacobi Gauss-Lobatto and equidistant grids can be constructed from first principles; if  $(x_j, j = 0, \dots, n)$  is the collocation grid chosen, the entries  $d_{ij}$  of the  $(0 : n) \times (0 : n)$  first-order derivative collocation matrix  $\mathcal{D}$ , derived analytically from the interpolating polynomial, are

$$d_{ij} = \frac{\prod_{k=0}^n (x_i - x_k)}{(x_i - x_j) \prod_{k=0, k \neq j}^n (x_j - x_k)}, \quad i, j, k = 0, \dots, n, \quad i \neq j \neq k, \quad (2.1)$$

$$d_{ii} = \frac{1}{\sum_{k=0}^n (x_i - x_k)}, \quad i, k = 0, \dots, n, \quad i \neq k. \quad (2.2)$$

These formulae result in the well-known ones if the analytically known Chebyshev Gauss-Lobatto grid  $(x_j = \cos j\pi/n, j = 0, \dots, n)$  is used (Canuto *et al.*, 1987). Values of order  $m$  derivatives on the collocation grid  $x_j$  are obtained by  $(\mathcal{D})^m$ .

As far as temporal discretization of (1.1) is concerned, the viscous nature of the problems in which we are interested introduces scales which dictate an implicit treatment of the linear term in this equation; the nonlinear term may be treated explicitly. Within the framework of solution methods which do not resort to splitting and introduction of intermediate fields but rather address the governing equations directly the combination of Crank-Nicholson (CN) with second-order Adams-Bashforth (AB2) or Runge-Kutta (RK) schemes has been extensively used for the time-integration of the viscous and the convective terms, respectively (Canuto *et al.*, 1987). However, the family of compact schemes proposed by P. R. Spalart *et al.* (1991) (SMR) presents more accurate and more stable alternatives to the CN-AB2 algorithm although it does not require additional computational effort to the latter scheme. The SMR algorithm may be written in compact form as

$$q''' = q'' + \Delta t \left\{ \mathcal{L}(\kappa q'' + \lambda q''') + \mu \mathcal{N}(q'') + \nu \mathcal{N}(q') \right\}, \quad (2.3)$$

where the superscript denotes fractional time-step,  $\mathcal{L}(q)$  and  $\mathcal{N}(q)$  are, respectively, the linear and nonlinear operators in the problem to be solved and  $\Delta t$  is the time-step. The rationale behind the derivation as well as sample values of the constants  $\kappa, \lambda, \mu$  and  $\nu$  of a self-starting SMR algorithm may be found in P. R. Spalart *et al.* (1991). The time-discretization of (1.1) using (2.3) delivers the following problem to be solved for  $(\zeta, \psi)$  at each fractional time-step

$$\mathcal{M}_1 \zeta''' = R, \quad (2.4)$$

$$\mathcal{M}_2 \psi''' + \zeta''' = 0, \quad (2.5)$$

where  $\mathcal{M}_1 = \partial^2/\partial x^2 + \partial^2/\partial y^2 - Re/(\lambda \Delta t)$  and  $\mathcal{M}_2 = \partial^2/\partial x^2 + \partial^2/\partial y^2$ , subject to the boundary conditions appropriate to the problem in consideration.  $R$  comprises the nonlinear and the terms arising from the discretization at previous fractional time-steps,

$$\begin{aligned} R = & -(\kappa/\lambda) \left[ \frac{\partial^2}{\partial x^2} + \frac{\partial^2}{\partial y^2} - Re/(\kappa \Delta t) \right] \zeta'' \\ & + (\mu Re/\lambda) (\psi_y'' \zeta_x'' - \psi_x'' \zeta_y'') + (\nu Re/\lambda) (\psi_y' \zeta_x' - \psi_x' \zeta_y'). \end{aligned} \quad (2.6)$$

The accuracy of the overall procedure clearly depends on the scheme utilised for calculation of the spatial derivatives. The spectral discretisation chosen introduces dense matrices and can only become competitive against other numerical approaches from the point of view of efficiency on account of the existence of a fast algorithm for the inversion of the implicit operators  $\mathcal{M}_1$  in (2.4) and  $\mathcal{M}_2$  in (2.5). While  $\mathcal{M}_2$  is time-independent, the first implicit operator is a function of a time-step  $\Delta t$  that is controlled by the Courant–Friedrich–Lewis condition and needs to be inverted at every time-step. If one sacrifices the advantage of an adjustable time-step and keeps  $\Delta t$  fixed at a slightly lower than its optimal value, a powerful EVD algorithm may be constructed for the efficient solution of the incompressible two-dimensional Navier–Stokes and continuity equations in streamfunction–vorticity formulation.

Key papers on EVD algorithms are the work of Haidvogel & Zang (1979) and that of Ku *et al.* (1987). The first authors discuss the solution of Poisson’s equation subject to homogeneous Dirichlet boundary conditions in transform space while the second authors present an eigenvalue decomposition algorithm for the Poisson equation resulting from a time-splitting of the incompressible Navier–Stokes and continuity equations in primitive-variables formulation in the context of real-space spectral collocation using Neumann boundary data. Here we present a variant of the EVD algorithm for the solution of the equations of motion in real-space using the streamfunction–vorticity formulation. Using this formulation within a direct, as opposed to time-splitting or iterative, time-integration methodology one Poisson and one Helmholtz problem are to be solved within each fractional time-step. This minimizes the necessary computing effort and makes the present algorithm one viable candidate to obtain the desired basic states.

#### (a) Single cavity, steady runs

Physical boundary conditions can only be provided for the stream-function  $\psi$  itself and its derivatives on the domain boundary. We refrain from discussion of the Ku *et al.* (1987) algorithm for the standard testbed lid-driven cavity problem, which we term EVD<sub>2</sub> for reasons which will become apparent in what follows, and concentrate on our novel EVD<sub>4</sub> algorithm which permits addressing problems in which both Dirichlet and Neumann boundary conditions are imposed on the stream-function while no boundary data are necessary for the flow vorticity. We take a rectangular cavity to be defined in the two-dimensional domain  $(x_i \in [0, AR], i = 0, \dots, m) \times (y_j \in [0, 1], j = 0, \dots, n)$ , where  $AR$  is the



aspect ratio of the cavity. The boundary conditions on  $\psi$  are

$$\psi_{in} = \psi_{0j} = \psi_{i0} = \psi_{mj} = 0, \quad (2.7)$$

$$(\partial^2 \psi / \partial y^2)_{in} = F(x_i), \quad (2.8)$$

$$(\partial \psi / \partial x)_{0j} = 0, \quad (2.9)$$

$$(\partial \psi / \partial y)_{i0} = 0, \quad (2.10)$$

$$(\partial \psi / \partial x)_{mj} = 0, \quad (2.11)$$

where  $f_{ij} \equiv f(x_i, y_j)$  represents either of  $\psi$  or  $\zeta$  grid-values at a fractional time-step and  $F(x)$  is a function used to distinguish between a constant-shear boundary condition,  $F(x) \equiv 1$ , and a function derived from the external boundary layer flow. The numerical discretisation of (2.4-2.5) leads to a system of simultaneous equations of the type

$$Mf + fN + cIf = g, \quad (2.12)$$

where  $M$  represents the  $(0 : m) \times (0 : m)$  discrete analogon of  $\mathcal{D}_x^2$ ,  $N$  represents the transpose of the  $(0 : n) \times (0 : n)$  discrete analogon of  $\mathcal{D}_y^2$ ,  $I$  is the identity matrix,  $c = -Re/(\lambda \Delta t)$  and  $g = R$  if (2.4) is being solved, while  $c = 0, g = -\zeta$  in the case of (2.5). On account of the homogeneous boundary conditions (2.7) on  $\psi$  (2.5) becomes

$$\sum_{i=2}^{m-2} M_{ki} \psi_{il} + \sum_{j=2}^{n-2} N_{lj} \psi_{kj} = -\zeta_{kl} - M_{k1} \psi_{1l} - M_{km-1} \psi_{m-1l} - N_{l1} \psi_{k1} - N_{ln-1} \psi_{kn-1}. \quad (2.13)$$

The boundary conditions (2.8-2.11) may be expressed using the discrete analoga  $X, Y$  and  $Y^2$  of the collocation derivative matrices  $\mathcal{D}_x, \mathcal{D}_y$ , and  $\mathcal{D}_y^2$ , respectively, as given by (2.1-2.2). It follows that

$$\psi_{1l} = \sum_{i=2}^{m-2} \delta_{1i} \psi_{il} \quad , \quad \psi_{m-1l} = \sum_{i=2}^{m-2} \delta_{m-1i} \psi_{il}, \quad (2.14)$$

$$\psi_{k1} = \bar{\kappa}_k + \sum_{j=2}^{n-2} \epsilon_{1j} \psi_{kj} \quad , \quad \psi_{kn-1} = \bar{\lambda}_k + \sum_{j=2}^{n-2} \epsilon_{n-1j} \psi_{kj}, \quad (2.15)$$

where  $\bar{\kappa}_k$  and  $\bar{\lambda}_k$  are used to impose the boundary condition on the lid,

$$\bar{\kappa}_k = \frac{-F_k Y_{0n-1}}{Y_{01} Y_{nn-1}^2 - Y_{n1}^2 Y_{0n-1}}, \quad \bar{\lambda}_k = \frac{F_k Y_{01}}{Y_{01} Y_{nn-1}^2 - Y_{n1}^2 Y_{0n-1}}, \quad (2.16)$$

and the vectors  $\delta_{1i}, \delta_{m-1i}$  and  $\epsilon_{1j}, \epsilon_{n-1j}$  are known functions of the entries of  $X, Y$  and  $Y^2$ ,

$$\delta_{1i} = \frac{X_{0m-1} X_{mi} - X_{mm-1} X_{0i}}{X_{01} X_{mm-1} - X_{m1} X_{0m-1}} \quad , \quad \delta_{m-1i} = \frac{X_{m1} X_{0i} - X_{01} X_{mi}}{X_{01} X_{mm-1} - X_{m1} X_{0m-1}}, \quad (2.17)$$

$$\epsilon_{1j} = \frac{Y_{0n-1} Y_{nj}^2 - Y_{nn-1}^2 Y_{0j}}{Y_{01} Y_{nn-1}^2 - Y_{n1}^2 Y_{0n-1}} \quad , \quad \epsilon_{n-1j} = \frac{Y_{n1}^2 Y_{0j} - Y_{01} Y_{nj}^2}{Y_{01} Y_{nn-1}^2 - Y_{n1}^2 Y_{0n-1}}. \quad (2.18)$$

The essence of the EVD<sub>4</sub> algorithm is to diagonalise the  $(0 : m-4)^2$  matrix  $\hat{M}$  and the  $(0 : n-4)^2$  matrix  $\hat{N}$  whose entries are

$$\hat{M}_{ki} = M_{ki} + M_{k1} \delta_{1i} + M_{km-1} \delta_{m-1i}, \quad k, i = 0, \dots, m-4, \quad (2.19)$$

$$\hat{N}_{lj} = N_{lj} + N_{l1} \epsilon_{1j} + N_{ln-1} \epsilon_{n-1j}, \quad l, j = 0, \dots, m-4. \quad (2.20)$$

The Poisson problem (2.13) becomes

$$\hat{M} f_{kl} + f_{kl} \hat{N} = -\zeta_{kl} - \hat{N}_{l1} \bar{\kappa}_k - \hat{N}_{ln-1} \bar{\lambda}_k = r_{kl}, \quad (2.21)$$

in which the non-singular matrices  $\hat{M}$  and  $\hat{N}$  may be diagonalised using their eigenvalue decomposition

$$\hat{M} = (M^*)\mu^*(M^*)^{-1} \quad \text{and} \quad \hat{N} = (N^*)\nu^*(N^*)^{-1}, \quad (2.22)$$

to yield

$$\mu^*(M^*)^{-1}f_{kl}(N^*) + (M^*)^{-1}f_{kl}(N^*) = (M^*)^{-1}r_{kl}(N^*). \quad (2.23)$$

As a consequence, instead of having to solve the  $(m-3) \times (n-3)$  system of simultaneous equations (2.21) one solves the  $(m-3) \times (n-3)$  algebraic equations

$$f^* = r^*/(\mu^* + \nu^*) \quad (2.24)$$

for  $f^* = (M^*)^{-1}f_{kl}(N^*)$ , given  $r^* = (M^*)^{-1}r_{kl}(N^*)$ . The structure of the EVD<sub>4</sub> algorithm is summarised in table 2. Clearly, the cost of this algorithm is a negligibly small fraction of the cost of a direct algorithm for the solution of the Poisson problem. This is documented in table 3 where memory and runtime requirements are shown for solution of (1.1-1.2) in the lid-driven cavity problem.

#### (b) Single cavity, unsteady runs

The algorithm of the previous section accounts for flow inside the cavity set up by a constant shear-driven flow in the (external) boundary-layer. However, on account of the first boundary condition in (2.7), exchange of fluid between the external flow and the cavity is prohibited. This can easily be (partly) remedied by specifying an alternative boundary condition at the North ( $N$ -)boundary of the cavity, which models unsteady motion generated by instability in the external flowfield. One such model of a boundary condition takes into account the fact that linear instability in the free-stream generates harmonic motion at this boundary. Compared with the previous section an analogous in spirit, if not in detail, algorithm can be constructed, in which small-amplitude perturbations in the boundary layer generate harmonic unsteadiness at the lip of the cavity. In turn, such a motion is modelled by imposition of the inhomogeneous boundary conditions

$$\psi_{in} = \varepsilon \cos(2\pi x_i) \cos(2\pi f t), \quad (2.25)$$

$$(\partial^2 \psi / \partial y^2)_{in} = 1 + \varepsilon \cos(2\pi(x_i + \phi_x)) \cos(2\pi f(t + \phi_t)) \quad (2.26)$$

to replace the first boundary condition in (2.7) and (2.8), respectively. Here  $\varepsilon \ll 1$  is a small-amplitude parameter,  $f$  is an imposed real frequency of the motion at the  $N$ -boundary, determined by matching with instability in the external flow (Duck, 2002) and  $\phi_x, \phi_t$  are constant phase-shift parameters in space and time, respectively.

The EVD<sub>4</sub> algorithm is consequently modified in order to account for the boundary conditions (2.25-2.26) while the last three of (2.7) and (2.9-2.11) are retained. The matrices  $\hat{M}$  and  $\hat{N}$  are then redefined to incorporate the unsteady boundary conditions, while  $\hat{M}$  and  $\hat{N}$  are identical with those in §2(a) in the limit  $\varepsilon = 0$ . In this manner the present algorithm generalises that of the previous paragraph without loss in efficiency or accuracy.

#### (c) Row of microcavities, unsteady runs

Finally, an integral part of the current research focusses on a coupled solution of the external boundary layer and the internal cavity flows. In this case a single-domain spectral spatial resolution, as used in the previous sections, is no longer appropriate. Alternative approaches for the numerical solution of such a problem include the spectral multidomain algorithm of Theofilis (2000a) or the spectral element methodologies of Dubois-P  lerin (1998) and Karniadakis & Sherwin (1999); the first two algorithms have been employed here.

The minimum nontrivial configuration of two microcavities embedded in the wall has been considered, as schematically depicted in figure 7. The horizontal wall is defined by  $y = 0$  while microcavities having length  $d$  and depth  $D$ , placed at a spacing  $s$  apart have been considered. Although this does not represent an essential constraint of the algorithms used, microcavities of identical dimensions have

been taken in order to reduce the number of free parameters in the problem; in the same spirit, unless otherwise stated, square microcavities ( $d = D$ ) have been considered throughout. In this manner, the remaining geometric parameters are the distance between the inflow boundary and the upstream corner of the first microcavity, that between the downstream corner of the second microcavity and the outflow boundary and, finally,  $y = H$ , representing the distance from the horizontal wall along the  $y$ -direction at which the integration domain is truncated. It is of interest to focus future research in studying the modifications to the solutions obtained herein when the present choice of parameters is altered, especially by considering identical cavities of different dimensions than those chosen here, or by considering microcavities that are mildly different to one-another, as the case is likely to be in practical applications.

Solutions obtained here have been confined to two spatial dimensions, but no assumption of periodicity at the inflow/outflow boundaries has been made; performance of a so-called 'spatial' direct numerical simulation (DNS) has been an explicit requirement in the early stages of designing the current project (Fedorov, personal communication). Both the spectral multidomain and the spectral element algorithm consider a partition of the configuration of figure 7 into a total of seven parent subdomains. The first algorithm proceeds by defining independent conforming two-dimensional canonical (global) mapped Chebyshev collocation grids to discretize each subdomain and an iterative procedure to ensure  $C^1$  continuity across domain interfaces. The second algorithm, still considers the same space tessellation but in addition permits independent prescription on the one hand of the number of regular subdomains into which each of the parent subdomains is partitioned and on the other hand the degree of the polynomial approximation within each subdomain. In this way, the spectral element approach has the potential to resolve large gradient regions, such as that near the corners at the lips of the microcavities, more efficiently than the global spectral multidomain approach. In both cases a semi-explicit time-integration scheme has been used, employing low-storage Runge-Kutta or backward-differences for the convective and Crank-Nicolson for the viscous terms. The boundary conditions used are

$$\text{At the walls : } u = v = 0, \quad (2.27)$$

$$\text{At inflow : } u = \frac{y}{H}U_\infty \quad (2.28)$$

$$v = 0, \quad (2.29)$$

$$\text{At } y = H : u = U_\infty, \quad (2.30)$$

$$v = 0, \quad (2.31)$$

$$\text{At outflow : } \text{stress} - \text{free conditions} \quad (2.32)$$

Note that (2.28), after adjustment of constants, is consistent with the constant-shear flow assumption used throughout this work.

### 3. Results

#### (a) Basic flow

##### (i) Single cavity, steady runs

The EVD algorithm discussed in § 2 (a) has been employed, replacing the uniform tangential velocity of the cavity roof (Theofilis, 2000a; Theofilis *et al.*, 2001) by that of uniform wall shear stress, as detailed. The issue of the singularity of the boundary conditions at the NE and NW corners of the cavity is thus absent in the present calculations and the time-accurate spectral collocation scheme utilized for the calculation of the basic flow demonstrates exponential convergence. Unlike the standard lid-driven cavity, in which the condition  $\psi_y = 1$  is imposed at the N boundary and defines the effective flow Reynolds number, there is some ambiguity in the definition of a Reynolds number in the present case. The input Reynolds number may be regarded as

$$Re = u_y(y = D)d^2/\nu, \quad (3.1)$$

given that in our approach the roof shear stress is constant (or  $\psi_{yy} = 1$ ); here  $\nu$  is the kinematic viscosity of the fluid. Two additional Reynolds numbers useful for closer comparisons with the standard lid-driven cavity problem may also be defined, namely an integral Reynolds number

$$Re_{\text{int}} = \frac{1}{\nu} \int_{x=0}^d u(x, y = D) dx, \quad (3.2)$$

as well as that based on the maximum streamwise velocity component attained at  $y = D$ ,

$$Re_{\text{max}} = \frac{1}{\nu} \max\{u(x, y = D)\}. \quad (3.3)$$

While  $\nu$  is a fixed parameter in the basic flow calculation code,  $u(x, y = D)$  is unknown *a priori* and is determined from the converged basic-flow field. Taking  $d = D = 1$  basic flow results have been obtained using a rectangular grid comprising upwards of 96 collocation points per spatial direction. These have been compared against the classic lid-driven cavity flow, the Reynolds number in the latter case taken to be of  $O(Re_{\text{int}})$  in the former. As an example a comparison between the constant-shear and lid-driven basic states in terms of the streamfunction  $\psi$ , the velocity components  $u = \psi_y, v = -\psi_x$  and the vorticity  $\zeta$  is shown in figure 2. The shear-driven cavity results have been generated using  $Re = 6250$ , which yields an effective Reynolds number of  $Re_{\text{int}} \approx 300$ . Both sets of the first three quantities and the vorticity of the shear-driven flow are presented by ten isolines between zero and the respective maxima. The comparison points to a general qualitative agreement between the two model flows. That the input Reynolds number ( $Re$ ) in the shear-driven case is substantially higher than  $Re_{\text{int}}$  shows how relatively ineffective the constant shear driving mechanism is. In anticipation of the parameter range necessary to produce globally unstable flows (Theofilis, 2000a; Theofilis *et al.*, 2001), constant-shear basic states were obtained at substantially larger values of the unit Reynolds number, as shown in figure 3. A monotonic increase of both  $Re_{\text{int}}$  and  $Re_{\text{max}}$  as  $Re = 1/\nu$  increases can be seen, which enhances the viscous assumptions discussed earlier. The extent to which the quantitative differences between the basic states modify the stability characteristics of the lid-driven cavity flow is examined in § 3 (b).

##### (ii) Single cavity, unsteady runs

Before doing so, though, basic flow results have been obtained using the DNS algorithm of § 2 (b). The objective has been to verify the ability of the code to couple unsteadiness generated by instability in the external field, which penetrates inside the microcavity, or unsteadiness due to resonance originating inside the microcavity which propagates in the boundary layer. As will be discussed in § 3 (b), this coupling is pivotal in order to combine the analytic/numeric approach of Duck (2002) in the external boundary layer flow with the present fully numerical approach required to describe flow inside the microcavity.

$t$	$\varepsilon$	$f$
$< 20$	0	0
$20 < t < 40$	$10^{-4}$	1
$40 < t < 60$	$10^{-4}$	0.5
$> 60$	0	0

Table 1. *Parameters for the single-cavity unsteady simulations*

To this end, a cavity of aspect ratio (depth over length) of 2 has been considered and constant parameter values  $\phi_x = \phi_t = 0$  have been used. The magnitude of the parameter  $\varepsilon$ , on the other hand, is expected to have a critical qualitative influence on the results of the simulations: taking a low value should result in *linear response* of the flow to the external forcing (see 2.25–2.26), where the imposed frequency  $f$  is in resonance with that by which the cavity responds; progressively increasing  $\varepsilon$  will result in departure from this behaviour towards nonlinearity.

Representative results of simulations are shown, in the form of time-dependence of a flow quantity at a given position in the flowfield in figure 4 (here  $u$  is monitored, although others exhibit qualitatively analogous behaviour) and in the form of the spatial distribution of  $\psi, u, v$  and  $\zeta$  at two characteristic times,  $t = 20$  and  $t = 40$ , in figures 5 and 6, respectively;  $\nu = 10^{-2}$ , i.e.  $Re = 100$  using the definition (3.1), and the parameters of table 1 have been used for these simulations. In figure 4 it can be seen that, starting from rest, at  $t < 20$  a steady state solution is approached; components of this solution are shown in figure 5. When non-zero amplitude forcing is applied at the  $N$  boundary of the cavity, the flow responds in a periodic manner as would be expected from (2.25–2.26). After rather short transients following the (Heaviside) changes of  $\varepsilon$  at  $t = 20$  and of  $f$  at  $t = 40$ , the flow settles to two different harmonic motions with periods  $T_{20-40} = 1/f = 1$  at  $20 \leq t < 40$  and  $T_{40-60} = 1/f = 2$  at  $40 \leq t < 60$ . Snapshots of the solution at  $t = 40$  are shown in figure 6. At  $t = 60$  the forcing is removed and, by the end of the simulation, the flow approaches the same steady-state reached at  $t = 20^-$ . At these parameters, this steady state corresponds to  $Re_{\text{int}} \approx 14$ .

Using the same parameter values but higher resolution has demonstrated convergence of the results presented and points to the reliability of the statements put forward in this section. Further, qualitatively analogous results obtained at parameter values different to those presented in table 1 point to the generality of the conclusions reached, namely that the imposition of harmonic motion at the open end of the cavity sets up a linear response of the flow inside the cavity in resonance with the imposed frequency, provided that the forcing amplitude  $\varepsilon$  is kept small. Another potentially significant result for subsequent modelling is the finding that the bulk of the fluid flow motion, both unforced and forced, is confined within a depth approximately equal to the length of the microcavity, as shown in the results of figures 5 and 6.

### (iii) *Two microcavities, unsteady runs*

Unsteady simulations have been performed, considering the entire flowfield which encompasses the near-wall part of the boundary layer and two microcavities embedded in the wall. Such simulations require orders-of-magnitude larger computing effort compared with the single-domain calculations and, hence, a limited amount of results monitoring variations of the essential flow parameters have been obtained. Nevertheless, these results suffice to highlight essential differences between the numerical solutions obtained in the previous two sections and the present more elaborate approach and point to the direction of future research. Specifically, two questions have been formulated and investigated:

- First, how does the flowfield in the near-microcavity region compare with solutions obtained numerically using the assumptions of the previous section, or those used in the analytic model of Fedorov & Malmuth (2001)?

- Second, how do the geometric parameters  $s$  (spacing between successive microcavities) and  $D$  (depth of a microcavity) affect the flowfield of a microcavity (including the induced boundary-layer flow) and the interaction of this flowfield with neighbouring microcavities?

Answers to these questions can provide guidance to theory and experiment alike. Further modelling can benefit from identification of the limitations, in terms of the minimum spacing/depth of microcavities, for which the integral conditions used in the analysis (Fedorov & Malmuth, 2001) hold, before interaction between the flowfields of the microcavities invalidates the assumption of isolated microcavities under which these integral conditions are derived. On the other hand, experiment can use information on the minimum spacing between microcavities when manufacturing materials whose stability properties are reliably predicted by theory. Clearly, a major unanswered question in this context is the influence of three-dimensionality on conclusions reached here. This is an issue that is partly addressed in § 3 (b) and should be further expanded in future work.

Taking  $L = d = D = 1$ , some numerical experimentation was necessary in order to determine the remaining geometric parameters, such that (a) the location of the inflow boundary does not interfere with the flowfield in the neighbourhood of the upstream microcavity, on the one hand permitting the boundary layer to develop on the upstream wall of the configuration and on the other hand not placing excessive resolution requirements on account of a long upstream domain, (b) the location of the outflow boundary be placed well downstream of the downstream cavity, such that the outflow boundary conditions are physically plausible and, finally, (c) the location at which the domain is truncated in the  $y$ -spatial direction be such that activity taking place in the neighbourhood of the microcavities is not affected by this (artificial) domain truncation.

Having ensured all three requirements, the remaining physical parameters with which numerical experiments were performed were the Reynolds number, defined as

$$Re = \frac{U_\infty d}{\nu}, \quad (3.4)$$

and the distance  $s$  between the microcavities. Additional numerical parameters that needed to be determined were the time-step  $\Delta t$  of the unsteady simulations and the number of subdomains in which each of the parent subdomains ( $p_1 - p_7$  in figure 7) was to be subdivided, as well as the degree of polynomial approximation within each subdomain. The last two parameters determine the convergence properties of the algorithm and the accuracy of the solutions obtained and are (alongside the Reynolds number) intimately linked with  $\Delta t$  via the CFL condition.†

Results have been obtained for  $Re \in [10, 10^3]$  and  $s \in [1, 4]$  while, in order to verify the conclusion put forward in the previous section regarding the significance of the microcavity depth parameter, simulations comparing the results of  $D = 1$  and 2, keeping all other parameters identical, have also been performed. In all calculations to be presented the spectral element code has been used, since it has been found that this methodology is substantially more efficient in resolving sharp gradients (such as those at the lips of the microcavities) by local refinement of the grid, as opposed to the spectral multidomain code in which such geometric singularities impose global requirements on the grid and, consequently, higher-than-necessary resolution away from the singularity. In this respect each of the 7 parent subdomains  $p_1 - p_7$  was further subdivided into  $4^2$  subdomains, within each of which flow quantities were resolved using a  $7^{th}$  degree polynomial. These values represent a compromise between accuracy and efficiency; resolving a parent subdomain using  $2^2$  subdomains and lower degree polynomials produces only qualitatively correct results, while further increasing the number of subdomains ( $6^2 \times 7 = 252$  being the next possibility, compared with the currently used  $4^2 \times 7 = 112$  subdomains) would be unnecessarily expensive. In the parameter ranges explored the unsteady algorithm has yielded stationary solutions only; at convergence successive time-step results exhibit a relative time variation of less than  $0.1 \times 10^{-6}$ .

Of the results obtained most relevant for the problem at hand, as has been stressed here and by Duck (2002), are low Reynolds number calculations. The spatial distribution of  $u(x, y)$  and  $v(x, y)$  at

† In the case of multidomain solutions the global spectral collocation grid utilised to resolve each parent subdomain is the only means of improving the solution accuracy.

$Re = 50$  and  $s = D = 1$  is presented in figure 8; the slow motion of flow inside the microcavity can be appreciated in this result. Closer examination of the normal (to the wall on which the boundary layer develops) velocity component reveals two interesting aspects of the flow. On the one hand, it can be seen that little communication takes place between fluid in the boundary layer and that in the cavity; fluid in the microcavity is found to be in near-solid-body rotation, as expected by the smallness of the Reynolds number. On the other hand, compensation of this phenomenon takes place in the boundary layer, where the presence of the microcavity appears to exert influence on the flow over a relatively large part of the domain outside the microcavity itself. The first result is in line with the assumption of the previous two paragraphs and those of Fedorov & Malmuth (2001) and Duck (2002). The second result is expected to have a strong influence on the stability characteristics of the boundary layer and can only be predicted numerically by simulations, such as these presented herein. Further inspection of the normal velocity component result appears to suggest that  $s = 1$  is a distance at which the fluid motion induced in the boundary layer by one microcavity interacts nonlinearly with that induced by its neighbour. In other words, placement of microcavities at distances  $s \leq 1$  apart will prohibit applicability to a row of microcavities (in an integral manner) of analytical models derived on the basis of a single microcavity. Next, the effect of  $s$  on the solutions obtained at constant  $Re$  and  $D$  is examined; representative results are presented in figure 9 at  $Re = 20, D = 1$ . It can be seen that  $s \geq 4$  is necessary in order for the induced flowfield of the downstream microcavity to become similar to that of the upstream microcavity. Unless three-dimensional instability modifies these basic flows, this result suggests that using such a spacing between microcavities can ensure that the model used to describe the induced flowfield of a single microcavity can be applied in an integral manner to describe the interaction between the boundary layer and a porous material. The Reynolds number effect on the conclusions put forward so far is next determined by obtaining solutions in the range of interest,  $Re \in [10, 20]$ , keeping  $s = 2, D = 1$ ; the results at the extreme Reynolds number values are presented in figure 10. It can be seen that, at least in the parameter ranges investigated, in which no unsteadiness occurs, the Reynolds number effect is substantially less pronounced than that of the spacing between microcavities. Finally, figure 11 essentially confirms the conclusions of the previous sections, namely that the bulk of the activity inside the microcavity takes place within a depth equal to the width of the microcavity; quantitative inspection of the solution in  $y \in [-2, -1]$  revealed a rapid decay of all flow quantities with depth. The results obtained have been analysed quantitatively in different ways, f.e. monitoring one-dimensional profiles of velocity components as a function of the wall-normal coordinate  $y$ . This task, however, is physically relevant only if three-dimensional instability does not destroy the two-dimensional basic states obtained; one means of addressing this instability is BiGlobal instability theory (Theofilis, 2002) to which we return now.

### (b) Global linear instability

Three-dimensionality can be introduced in the results of the previous section by receptivity, followed by either linear instability or transient growth. Examination of all relevant mechanisms is beyond the scope of the present work; focussing on BiGlobal linear instability, one result that may be inferred from the steadiness of the basic states obtained is that the two-dimensional BiGlobal eigenmode ( $\beta = 0$ ) is stationary (Theofilis, 2000b). On the other hand, linear amplification of three-dimensional BiGlobal eigenmodes (having  $\beta \neq 0$ ) can be examined by numerical solution of the partial derivative eigenvalue problem (1.5–1.8).

At present, only single-domain solutions of the EVP have been obtained, using the steady basic states calculated in § 3 (a) (i) and monitoring the relative stability properties of shear-driven and lid-driven cavity flow. The straightforward viscous boundary conditions on the disturbance velocity components have been imposed on the three solid walls, while the issue of boundary conditions on the  $N$ -boundary of the shear-driven cavity is expected to be the key linking the flowfield of an isolated microcavity with that prevailing in the external flow, studied by Duck (2002). In the absence of prior information, calculations reported here have been performed by imposing homogeneous Dirichlet or extrapolation of the disturbance velocity components from the cavity interior; appropriate compatibility conditions for the disturbance pressure have been used to close the system to be solved in both cases. In the framework of a temporal global instability analysis the only parameters of the problem are the flow

Reynolds number  $Re$  and the spanwise periodicity length  $L_z$ , associated with a wavenumber  $\beta = 2\pi/L_z$ , while the complex temporal eigenvalue  $\Omega$  and the two-dimensional amplitude functions  $(\hat{u}, \hat{v}, \hat{w}, \hat{p})^T$  of the disturbance quantities are determined by the numerical solution of the partial-derivative eigenvalue problem.

At  $Re_{\text{ldc}} = Re_{\text{int}} \approx 300$  the lid-driven cavity flow is known to be stable to both two- and all three-dimensional perturbations. Comparisons between the two model flows are only possible in the case of homogeneous Dirichlet boundary conditions being imposed at the N boundary in the shear-driven case. The modification of the (least damped) leading eigenvalues of the eigenspectrum at  $\beta = 7.5$  (approximately corresponding to least-damped conditions for mode T2 (Theofilis, 2000a; Theofilis *et al.*, 2001)) is shown in the upper part of figure 12. Owing to the disparity between  $Re_{\text{ldc}}$  and  $Re$  the shear-driven flow experiences much weaker damping compared with its lid-driven counterpart. Noteworthy is also the difference between the two flows in terms of the prevalence of stationary and low-frequency disturbances (in the neighbourhood of  $\Omega_r = 0$ ) in the shear-driven cavity case at  $Re = 6250$ . At  $Re = 25 \times 10^4$ , on the other hand, the flow is marginally unstable at  $\beta = 7.5$ ; the corresponding spectrum is shown in the lower part of figure 12. The amplitude function of the spanwise disturbance velocity component  $\hat{w}$  and the disturbance pressure  $\hat{p}$  of the unstable global eigenmode is shown in figure 13. The complexity of the (periodic in  $z$ ) flowfield, setup by global instability inside the microcavity, can be seen in this figure, while the analogies of the structure of the global eigenmode with that in the lid-driven cavity (Theofilis, 2000a; Theofilis *et al.*, 2001) can also be appreciated.

The currently imposed boundary condition of impermeability at the roof of the cavity has been extended to that suggested by Duck (2002),

$$\hat{v} - \Lambda \hat{p} = 0, \quad (3.5)$$

which can provide the link between the external and internal disturbance flowfields. However, in view of the basic flow results of § 3 (a) (iii), further stability calculations have not been performed until the issue of the appropriate basic state to be used for such stability calculations has been addressed in a satisfactory manner, a task constituting one of the possible interesting extensions of the present effort.



#### 4. Conclusions

This report may be regarded as a first step in modelling the flow inside porous media coatings which are known to be useful in controlling hypersonic (in particular mode II) boundary-layer flow instabilities. The practically incompressible nature of the flow inside the microcavities strongly suggests that temperature perturbations in the outer flow are unlikely to be substantially affected by the presence of the microcavities.

The first set of results obtained has assumed the outer flow to affect the inner (cavity) flow, but not vice-versa. The nature of two-dimensional basic flow inside a microcavity driven by a uniform shear-stress on one face was established by use of an accurate and efficient eigenvalue decomposition algorithm (EVD) for direct numerical simulation. Details of the novel aspects of the EVD algorithm have been presented. Some BiGlobal instability results of this flow have also been obtained; they strongly suggest the flow to be quite stable in likely practical regimes (Reynolds numbers), particularly when compared with the lid-driven cavity problem (Theofilis, 2000a; Theofilis *et al.*, 2001).

The second set of results obtained has permitted small-amplitude harmonic perturbations superimposed upon the solutions obtained in the first leg of the investigations. An isolated microcavity has been shown to respond to external forcing in a linear manner, periodic flow being set up inside the cavity at the imposed external frequency. This extension is necessary in order to permit a more interactive regime, especially with respect to the perturbed flow. In particular a more realistic boundary condition recently suggested by Duck (2002) can be used to relate the wall-normal component of the disturbance velocity and disturbance pressure on the external face of the cavity, as derived from the present numerical approach, with those of the external flowfield analysed by Duck (2002).

Finally, the basic flow results obtained using the previous two sets of approximations have been put in perspective by performing (unsteady) DNS of the entire flowfield, which encompasses both the near-wall boundary layer and two microcavities embedded in the wall. It has been shown that the parameter on which the flowfield most critically depends on is the spacing between microcavities; beyond a spacing  $s \approx 4$  (which scales with other geometric parameters of the flow) it appears to be permissible to study microcavities in isolation from each other (but interacting with the boundary layer) and calculate the effect of the induced flow motion on the boundary layer in an analytical (integral) manner. Other parameters, such as the depth of the cavities and the Reynolds number have been found to have a lesser impact on the flow, at least in the parameter range of interest where steady states prevail.

Future work aiming to aid optimization of the process of microcavity scale and distribution should address the key issue left open in the current investigations, namely three-dimensionality. This can be studied either as harmonic modification in the third spatial direction of the present (single- and multiple-microcavity configuration) two-dimensional basic states or through consideration of essentially inhomogeneous three-dimensional microcavities of different geometric characteristics embedded in the boundary layer.

## References

- CANUTO, C., HUSSAINI, M. Y., QUARTERONI, A. & ZANG, T. A. 1987 *Spectral methods in fluid dynamics*. Springer.
- DUBOIS-PÉLERIN, Y. 1998 SPECULOOS: An object-oriented toolbox for the numerical solution of partial differential equations by the spectral and mortar element method. *Tech. Rep.* DGM-LMF T-98-5. Ecole Polytechnique Fédérale de Lausanne.
- DUCK, P. W. 2002 Theoretical prediction of the hypersonic boundary-layer over a row of microcavities. *Tech. Rep.* F61775-01-WE049. EOARD.
- FEDOROV, A. V. & MALMUTH, N. D. 2001 Stabilization of hypersonic boundary layer by porous coatings. *Tech. Rep.* 2001-0891. AIAA.
- HAIDVOGEL, D. B. & ZANG, T. A. 1979 The accurate solution of Poisson's equation by expansion in Chebyshev polynomials. *J. Comp. Phys.* **39**, 167–180.
- KARNIADAKIS, G. E. & SHERWIN, S. J. 1999 *Spectral/hp element methods for CFD*. OUP.
- KU, H. C., HIRSCH, R. S. & TAYLOR, T. D. 1987 A pseudospectral method for solution of the three-dimensional incompressible Navier-Stokes equations. *J. Comput. Phys.* **70**, 549–462.
- P. R. SPALART, R. D. MOSER & M. M. ROGERS 1991 Spectral methods for the Navier-Stokes equations with one infinite and two periodic directions. *J. Comput. Phys.* **96**, 297–324.
- RASHEED, A., HORNUNG, H. G., FEDOROV, A. & MALMUTH, N. 2001 Experiments on passive hypervelocity boundary-layer control using a porous surface. *Tech. Rep.* 2001-0274. AIAA.
- THEOFILIS, V. 2000*a* Globally unstable basic flows in open cavities. *Tech. Rep.* 2000-1965. AIAA.
- THEOFILIS, V. 2000*b* On steady laminar basic flows and their global eigenmodes: An elliptic cone in compressible flow. *Tech. Rep.* F61775-99-WE049. EOARD.
- THEOFILIS, V. 2002 Advances in global linear instability theory. *Prog. Aero. Sci.* p. (to appear).
- THEOFILIS, V., DUCK, P. W. & OWEN, J. 2001 Global viscous linear stability of three classes of rectangular duct flows. *J. Fluid Mech.* p. submitted.

## 1 Pre-processing Stage

- a. Set up the matrices  $\hat{M}$  and  $\hat{N}$ ,  
calculate their EVD and store the results
- b. Set up the matrices  $\tilde{M}$  and  $\tilde{N}$ ,  
calculate and store their EVD

## 2 Time-advancement

## i. First fractional time-step

- a. Given an initial  $\psi''$  calculate  $\zeta'' = -\nabla^2 \psi''$   
or read-in  $(\psi'', \zeta'')$  data generated at an earlier simulation
- b. Calculate derivatives of  $\psi''$  and  $\zeta''$  and form  $R$
- c. Use EVD<sub>2</sub> to solve  $\nabla^2 \zeta''' = R$
- d. Use EVD<sub>4</sub> to solve  $\nabla^2 \psi''' = -\zeta'''$
- e. Overwrite  $(\psi', \zeta')$  by  $(\psi'', \zeta'')$  and  $(\psi'', \zeta'')$  by  $(\psi''', \zeta''')$  respectively

## ii. Second fractional time-step

- a. Given  $\psi'', \zeta'', \psi'$  and  $\zeta'$  calculate their derivatives and form  $R$
- c. Use EVD<sub>2</sub> to solve  $\nabla^2 \zeta''' = R$
- d. Use EVD<sub>4</sub>to solve  $\nabla^2 \psi''' = -\zeta'''$
- e. Overwrite  $(\psi', \zeta')$  by  $(\psi'', \zeta'')$  and  $(\psi'', \zeta'')$  by  $(\psi''', \zeta''')$  respectively

## iii. Third fractional time-step

- a.-e. Same as 2 ii.

## iv. Check convergence in time and either Go To 2 i. or Exit

Table 2. *An algorithm for the solution of the two-dimensional incompressible Navies–Stokes and continuity equations using the streamfunction–vorticity formulation and eigenvalue decomposition*

problem size	SUN Sparc 10				NEC SX4			
	EVD		direct inversion		EVD		direct inversion	
	size (Mb)	time (sec)	size (Mb)	time (sec)	size (Mb)	time (sec)	size (Mb)	time (sec)
$16 \times 16$	0.4	4.4	1.1	3.7	4.03	0.03	4.03	0.1
$24 \times 24$	0.5	5.4	3.6	10.5	5.03	0.14	6.03	0.3
$32 \times 32$	0.6	6.6	10.0	39.7	5.03	0.25	13.03	1.1
$48 \times 48$	0.8	15.3	46.9	460.6	6.03	0.56	48.03	8.4
$64 \times 64$	1.1	31.8	143.9	5203.5	6.03	1.08	140.03	40.7
$96 \times 96$	1.8	143.3	(*)	(*)	8.03	2.48	680.03	417.4
$128 \times 128$	2.8	523.1	(*)	(*)	8.03	4.41	(*)	(*)

Table 3. Comparison of memory and runtime requirements for a single solution of a two-dimensional Poisson equation using direct inversion and the  $EVD_4$  algorithm on one processor of a workstation and a supercomputer. Asterisks denote that the respective problem does not fit in the available memory on the workstation or that it cannot be solved within the existing batch queue time-limit on the supercomputer.

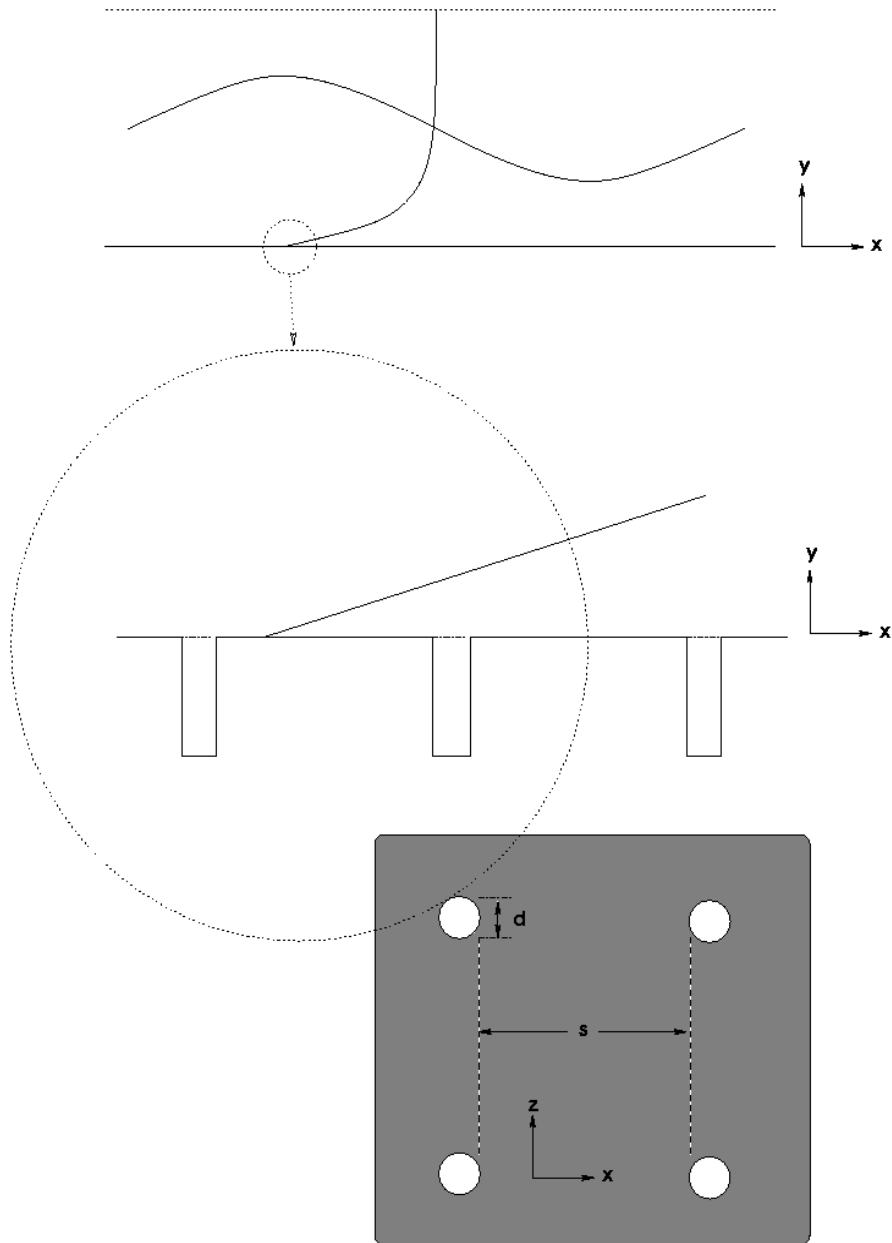


Figure 1. Schematic representation of the modelled geometry

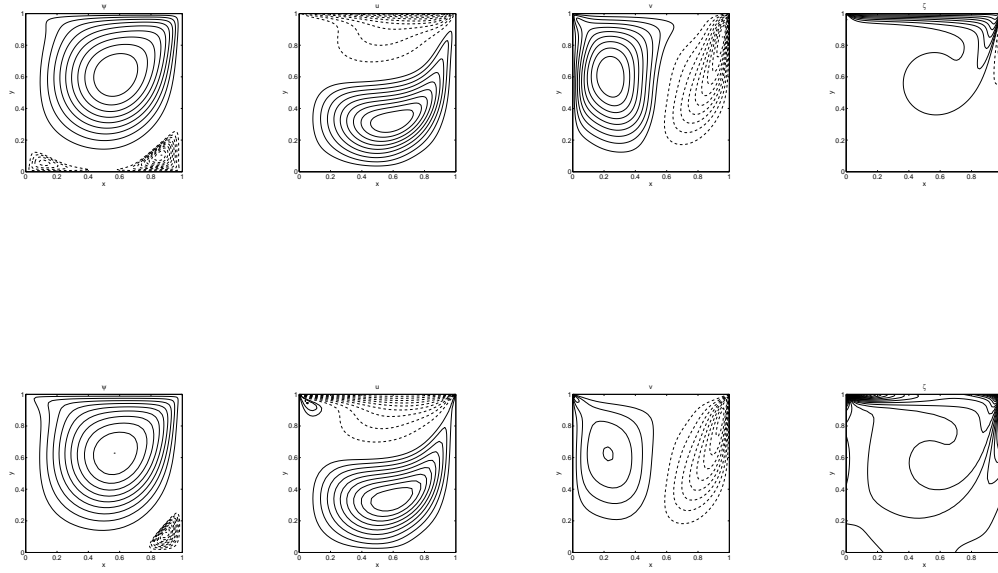


Figure 2. Comparison of the basic states for the shear-driven at  $Re_{\text{int}} = 300$  (upper row) and the lid-driven cavity flow at the same Reynolds number (lower row). Left to right column:  $\psi, u, v, \zeta$ .

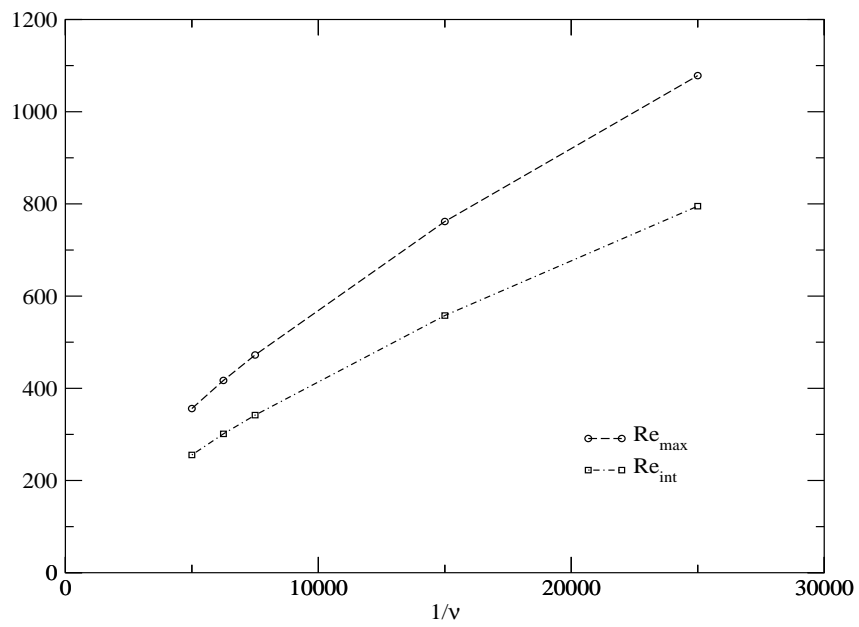


Figure 3. Dependence of  $Re_{\text{int}}$  and  $Re_{\max}$  on  $1/\nu$  in a square shear-driven cavity.

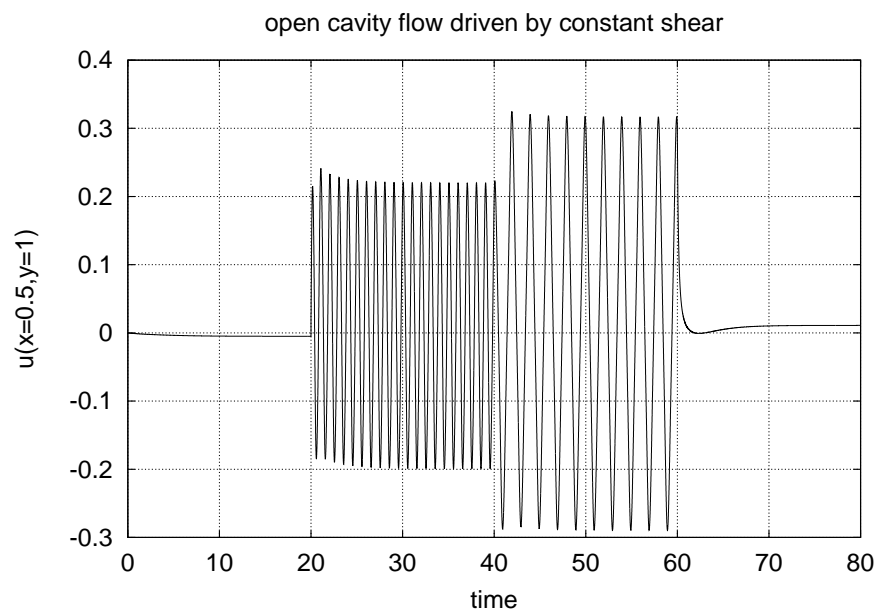


Figure 4. Periodic flow set up inside an aspect-ratio-two microcavity, as a consequence of a shear which is harmonically-dependent on time; shown is  $u(x = 0.5, y = 1; t)$ .



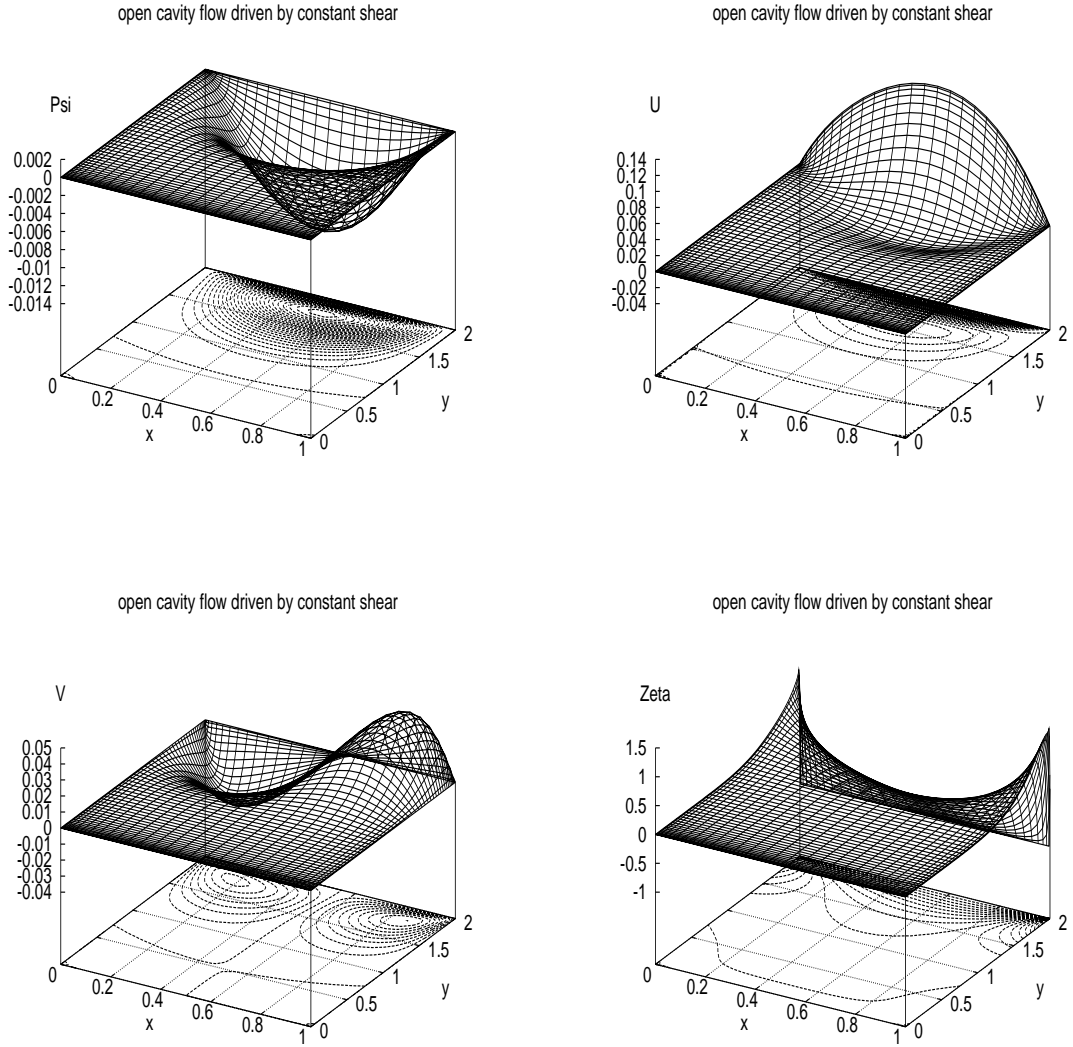


Figure 5. The steady-state solution approached at  $t = 20^-$ . Components shown are  $\psi$  (upper left),  $u$  (upper right),  $v$  (lower left),  $\zeta$  (lower right).

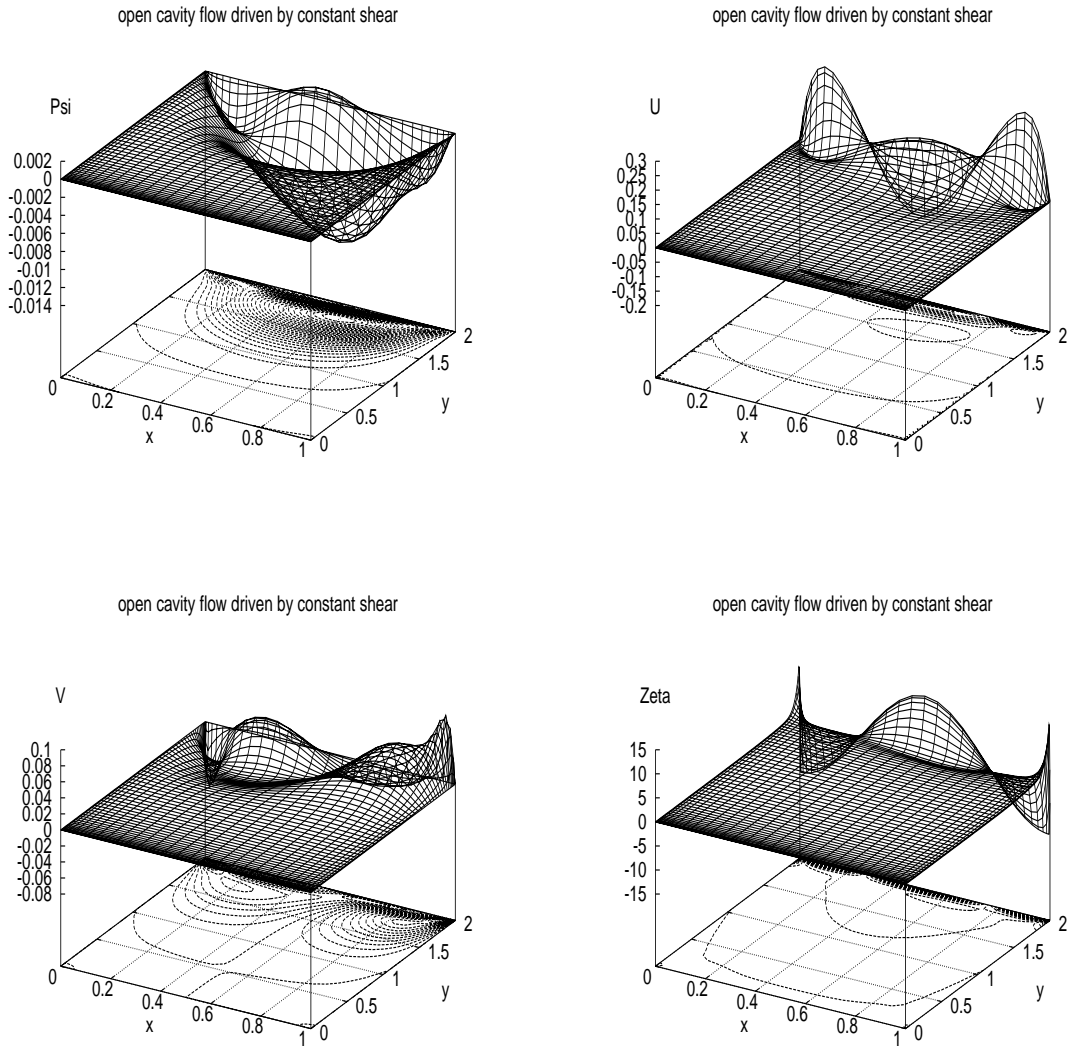


Figure 6. Snapshots, at  $t = 40$ , of the periodic flowfield set up inside the microcavity by harmonic motion at the cavity lip. Components shown are  $\psi$  (upper left),  $u$  (upper right),  $v$  (lower left),  $\zeta$  (lower right).

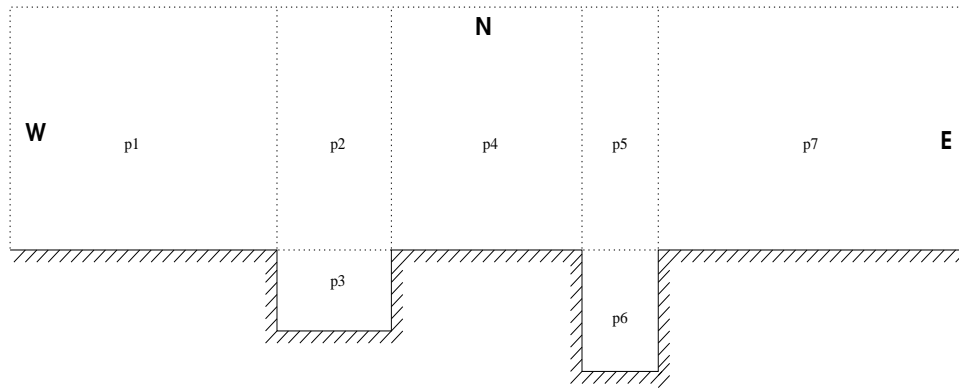


Figure 7. Sketch of the geometry considered.

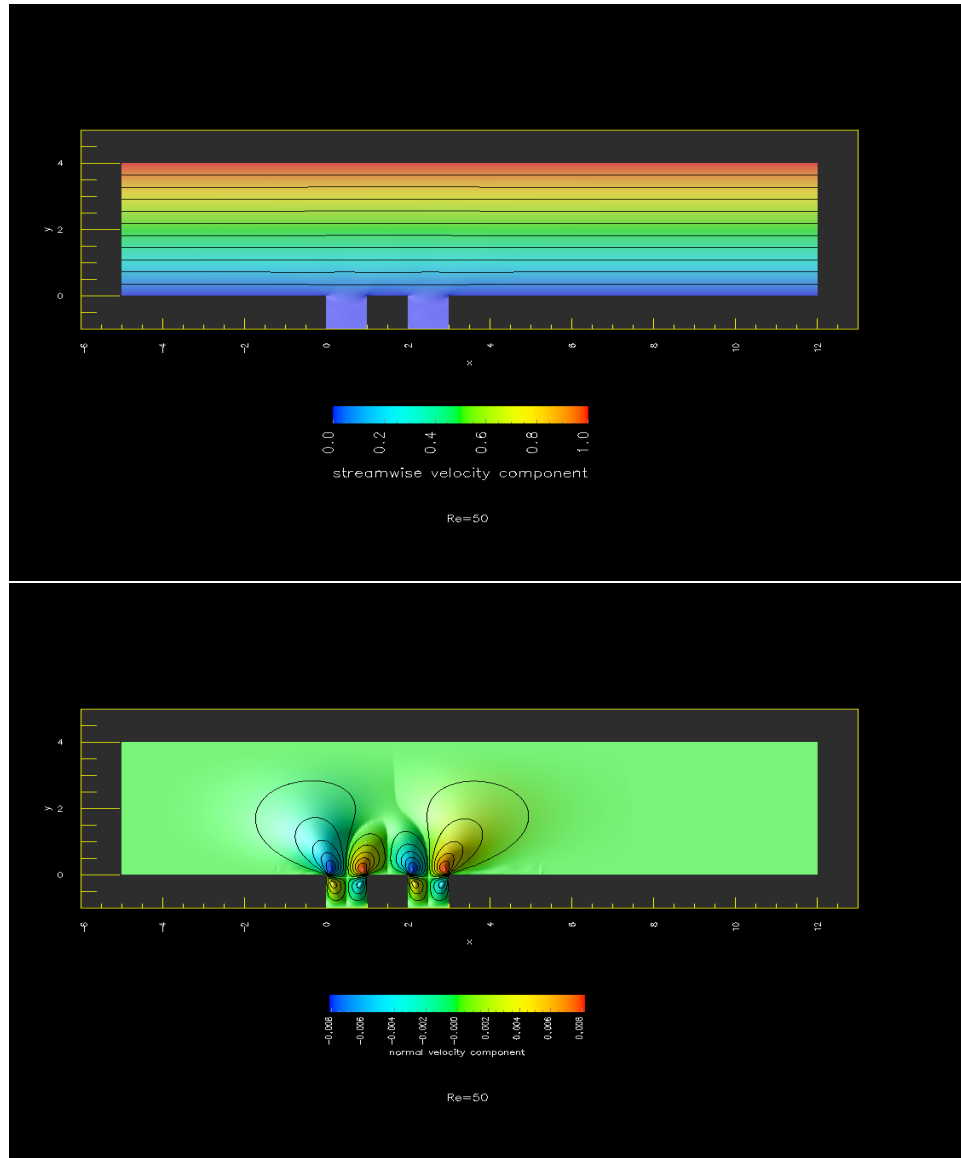


Figure 8.  $Re = 50$  flow over two unit square microcavities, set apart by  $s = 1$ . Upper: streamwise velocity component; lower: normal velocity component.

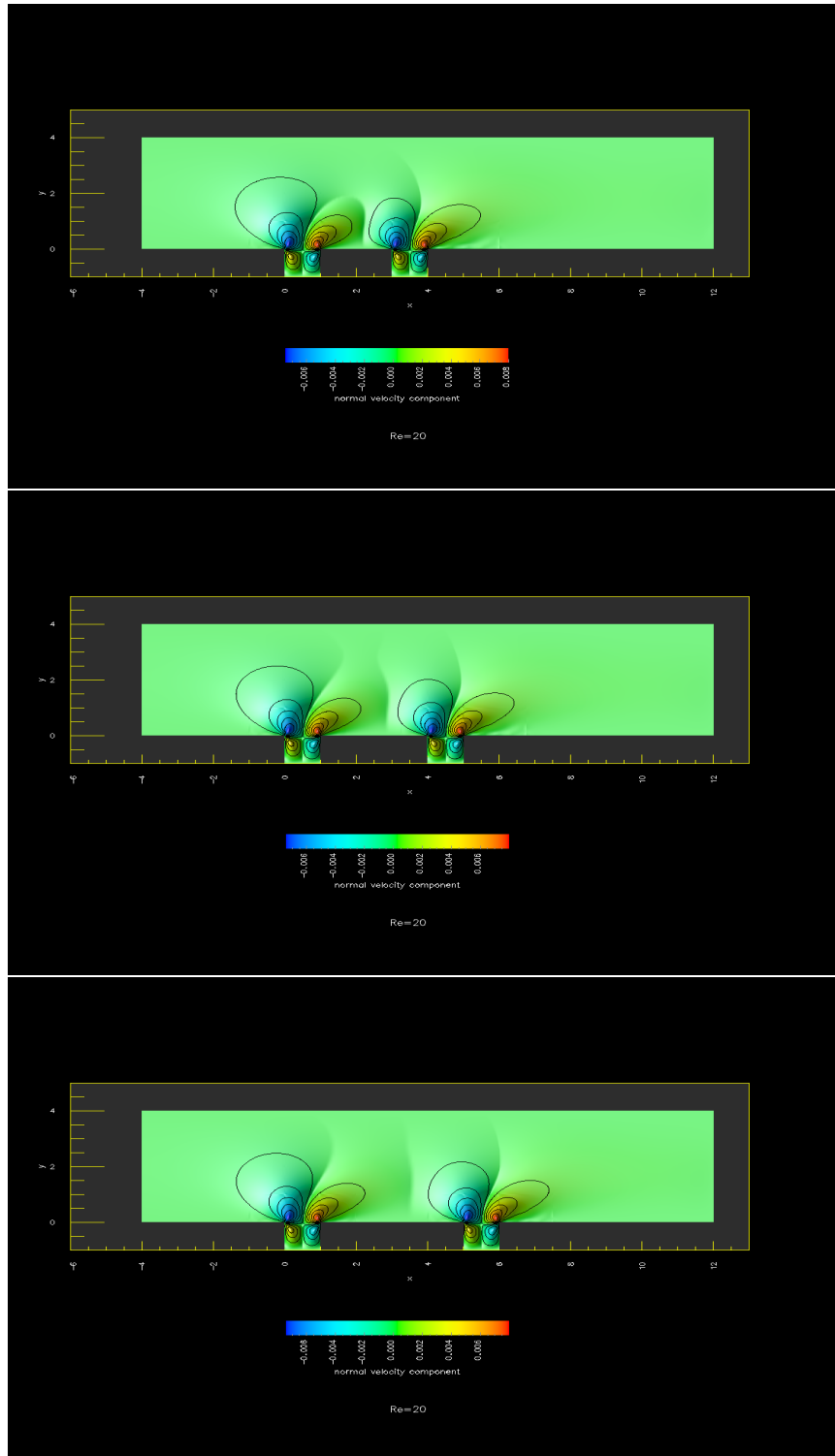


Figure 9. Effect of spacing  $s \in [2, 4]$  on a two-unit-square-microcavity configuration at  $Re = 20$ .

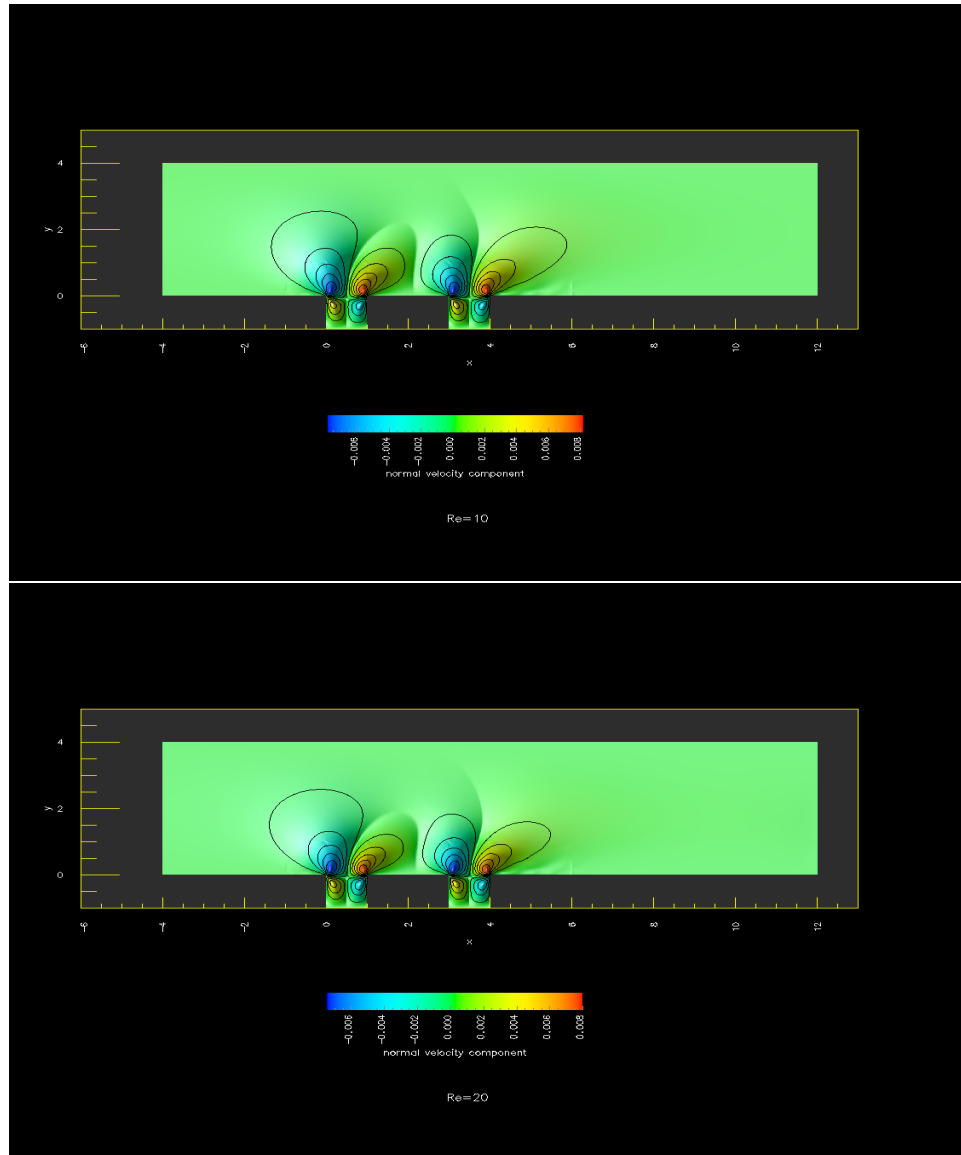


Figure 10. Reynolds number effect on the normal velocity component in a two-unit-square-microcavity configuration at  $s = 2$ .

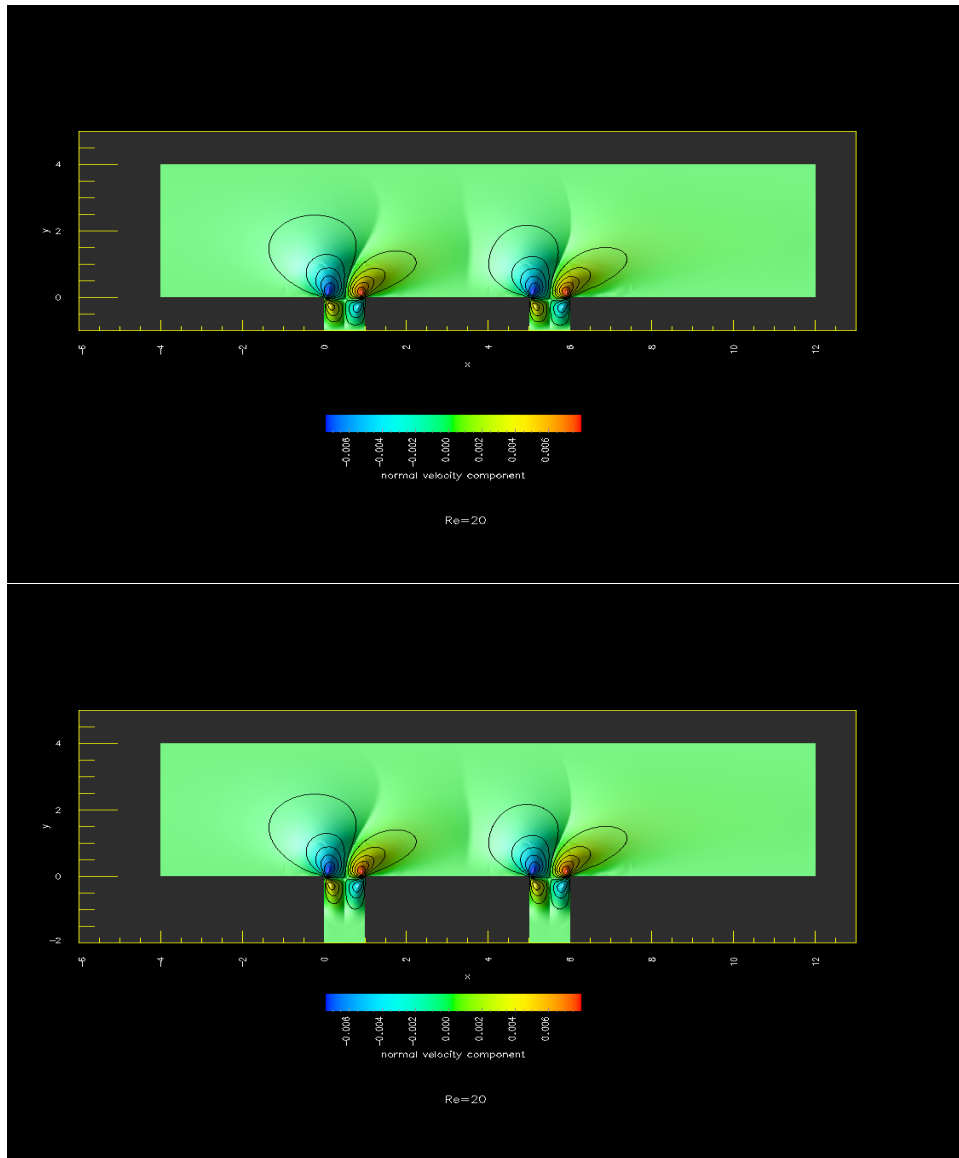


Figure 11. Effect of depth  $D = 1$  and 2 on in a two-microcavity configuration at  $Re = 20, s = 2$ .

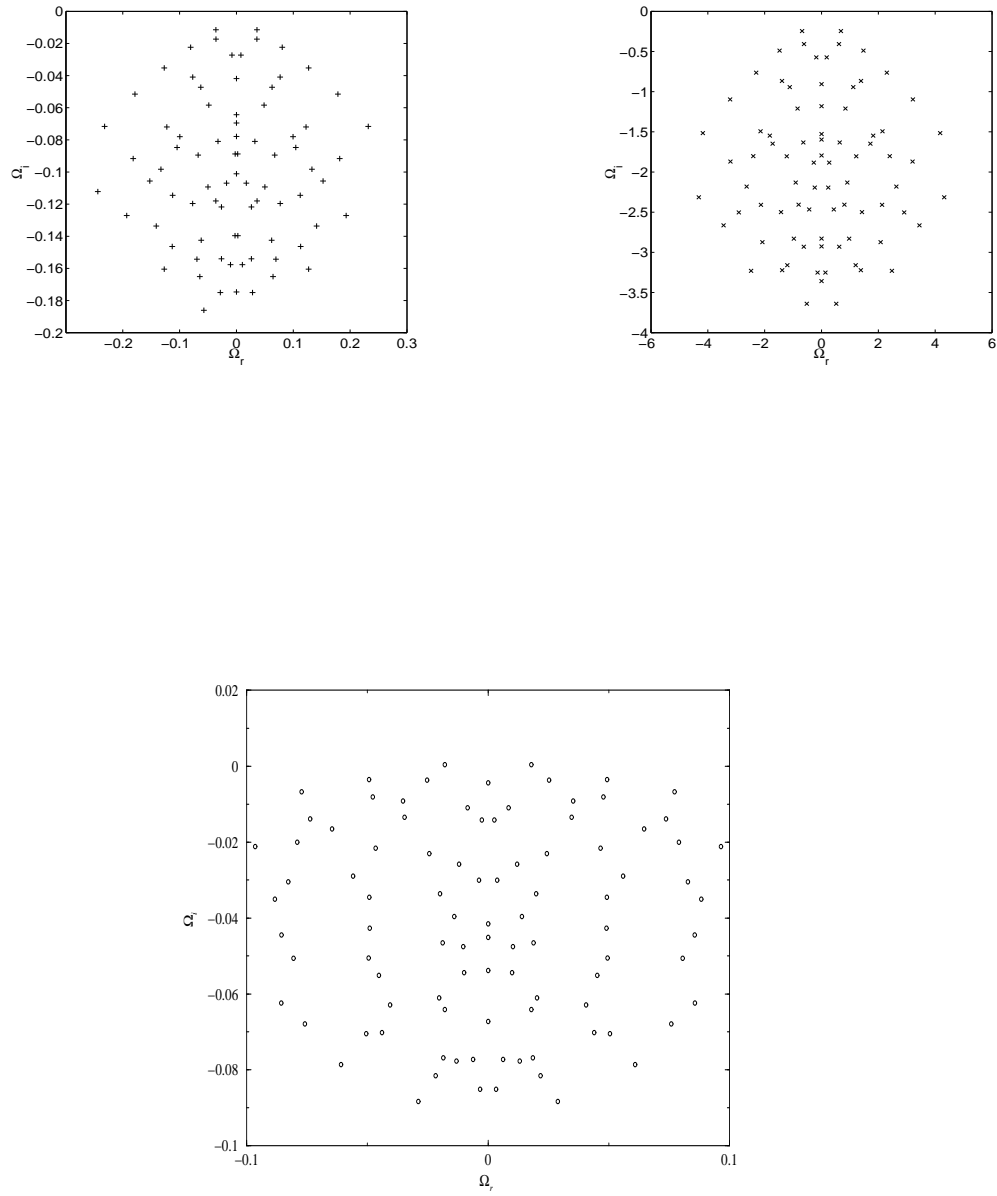


Figure 12. Upper: Comparison of the global eigenspectra in the shear-driven (+) and the lid-driven cavity (x) at  $Re = 300$ . Lower: Unstable spectrum in the shear-driven cavity at  $Re = 25 \times 10^4$



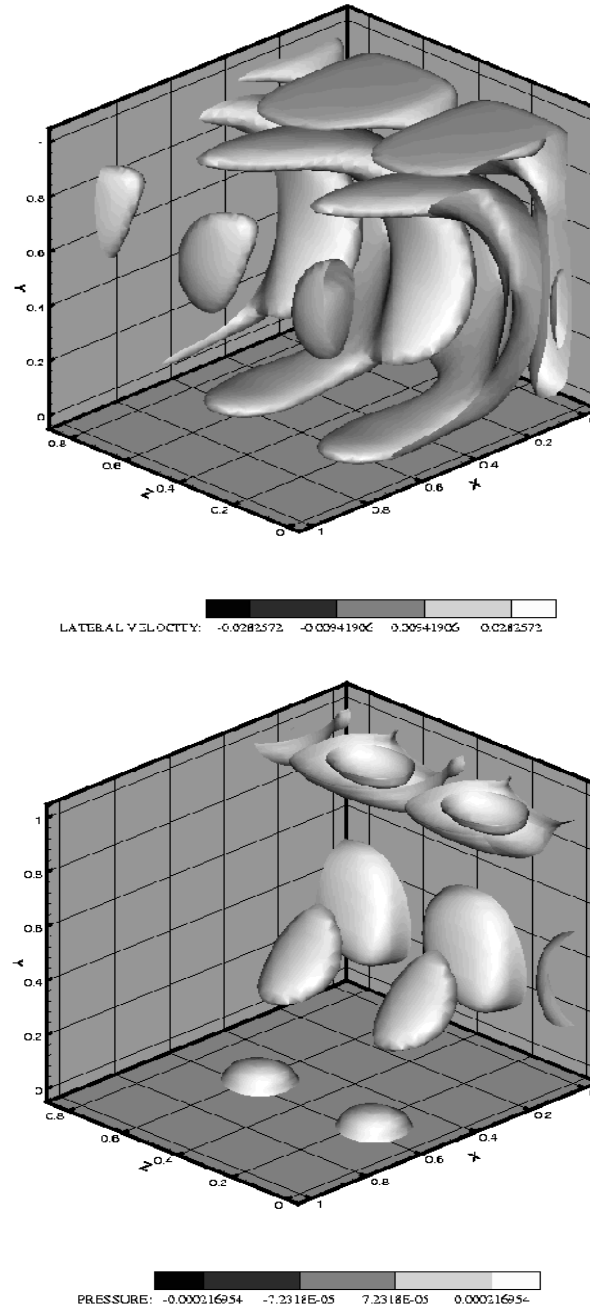


Figure 13. Four isosurfaces of the spanwise disturbance velocity component (upper) and disturbance pressure (lower) generated by global instability inside a square microcavity at  $(Re = 25 \times 10^4, \beta = 7.5)$ . Levels are equidistributed between the respective minimum and maximum values.

Nomenclature associated with the Final Report

**F61775-01-WE049**

*Numerical Prediction of the Hypersonic Boundary-Layer Over a Row of Microcavities*

by

V Theofilis

<b>Latin Symbols</b>	
d, D	2D microcavity width, depth
f	(dimensionless) frequency
H	2D microcavity domain height
Re	Reynolds number
t	time
x, y	Cartesian coordinates/ collocation points
u, v, w	Cartesian velocity components
<b>Greek Symbols</b>	
$\beta$	Spanwise wavenumber
$\Delta t$	Timestep
$\varepsilon$	Small-amplitude parameter
$\kappa, \lambda, \mu, \nu$	Time-integration constants
$\phi$	Phase-shift parameter
$\psi, \omega$	Stream-function, vorticity
$\Omega$	Complex eigenvalue of the global eigenvalue problem
$\Omega_r$	Real BiGlobal frequency
$\Omega_i$	Real BiGlobal amplification/damping rate
<b>Calligraphic symbols</b>	
D	(analytic) collocation derivative
$K, L, M, N$	Linear operators
<b>Superscripts</b>	
$\cdot, \cdot', \cdot''$	Fractional timestep quantity
–	Basic flow quantity
$\hat{\cdot}, \sim$	Disturbance flow quantity
*	Eigenvalue vector
<b>Subscripts</b>	
i, j, k, l, m, n	(discrete) indices